

1 Seismic anisotropy under Zagros foreland from SKS splitting observations

2 Khalil Motaghi¹, Ayoub Kaviani², Wathiq Abdalnaby³, Hanan Mahdi⁴, Haydar Al-Shukri⁴

3 ¹Department of Earth Sciences, Institute for Advanced Studies in Basic Sciences (IASBS), Zanjan 45137-66731,
4 Iran

5 ²Institute of Geosciences, Goethe University, Frankfurt, Germany

6 ³Seismological Laboratory of University of Basrah (SLUB), Department of Geology, College of Science,
7 University of Basrah, Basrah, Iraq

8 ⁴University of Arkansas at Little Rock (UALR), Little Rock, Arkansas, US

9 **Correspondence:** Khalil Motaghi (khalil1024@yahoo.com)

10 Abstract

11 We present SK[K]S splitting measurements from 18 newly deployed seismic stations in the
12 foreland of the Zagros collision zone, providing new insights into asthenospheric flow and
13 lithospheric deformation associated with the Arabian-Eurasian continental collision. Our
14 results reveal two distinct fast-axis orientations: NE-SW in northern Iraq and NW-SE in the
15 Mesopotamian Plain and Persian Gulf. The NE-SW anisotropy in northern Iraq aligns with
16 fast-axis orientations observed in the Iranian-Anatolian Plateau and the azimuth of absolute
17 plate motion, indicating large-scale asthenospheric flow as the primary **cause of anisotropy**
18 across the northern Middle East. In contrast, the **NW-SE-trending** anisotropy in the
19 Mesopotamian Plain and Persian Gulf, characterized by smaller splitting times, **is parallel to**
20 **the** previously reported Pn anisotropy, suggesting a contribution from lithospheric mantle
21 anisotropy, likely **preserved as** a remnant of past rifting. The influence of asthenospheric flow
22 on the observed seismic anisotropy in this region appears minor. **These findings demonstrate**
23 **a dual origin of seismic anisotropy in the Zagros foreland, where lithospheric fabric related to**
24 **Mesozoic rifting dominates in the Mesopotamian Plain, southwest of the Zagros lithosphere**

25 keel, while asthenospheric flow governs the anisotropy in northern Iraq and surrounding
26 regions with thin lithosphere. This distinction refines models of mantle dynamics and
27 lithosphere-asthenosphere coupling in continental collision zones.

28 **Keywords:** Anisotropy, Zagros collision, Mesopotamia, Asthenospheric flow, SK[K]S

29

30 **1. Introduction**

31 Seismic anisotropy is a powerful tool for probing the dynamics of the Earth's mantle and
32 understanding the processes that drive plate tectonics (e.g., Park and Levin, 2002; Long and
33 Becker, 2010). It provides critical insights into deformation within the crust and upper mantle
34 and can reveal deep structural features, such as mantle flow, that are often inaccessible to
35 other geophysical methods (Silver and Chan, 1991).

36 This study focuses on the foreland region of the Zagros continental collision zone, a key
37 segment of the Arabia–Eurasia plate boundary. Here, we investigate the interaction between
38 asthenospheric mantle flow and the overlying continental lithosphere, particularly the
39 influence of the thick lithospheric root beneath the Zagros orogen (Priestley et al., 2012).
40 These interactions are shaped by large-scale plate motions and localized mantle dynamics,
41 including shear and normal tractions at the base of the lithosphere (Sandvol et al., 2003).
42 Despite the tectonic significance of the region, the Zagros foreland remains underexplored
43 due to limited seismic station coverage.

44 Teleseismic shear-wave splitting offers a sensitive method for detecting anisotropy within
45 both the lithospheric and asthenospheric mantle (Silver and Holt, 2002). In the broader
46 Middle East, SK[K]S splitting studies have revealed a consistent NE-oriented fast axis
47 beneath northern Iran and Anatolia, interpreted as reflecting asthenospheric flow aligned with

48 the absolute plate motion (APM) in a no-net-rotation frame (Paul et al., 2014; Arvin et al.,
49 2021; Kaviani et al., 2021). In contrast, the anisotropy pattern across the Zagros is more
50 complex, influenced by deformation of the thick Arabian lithosphere (Sadegh-Bagherabadi et
51 al., 2018b) and lateral variations in lithospheric thickness, which may deflect or suppress
52 asthenospheric flow (Kaviani et al., 2021).

53 Despite these advances, the foreland basin beneath eastern Iraq and the Persian Gulf remains
54 poorly characterized. This is largely due to logistical constraints: the partial overlap of the
55 region with the Persian Gulf limits onshore station coverage, and eastern Iraq has historically
56 lacked adequate seismic monitoring (Fig. 1). As a result, it has been difficult to resolve
57 whether anisotropy in this region reflects present-day mantle flow or inherited lithospheric
58 structure.

59 To address this gap, we analyze new data from 17 seismic stations in Iraq and one recently
60 deployed station on an island in the Persian Gulf. The Iraqi stations, installed as part of a
61 network enhancement initiative led by Lawrence Livermore National Laboratory, offer the
62 first opportunity to investigate anisotropic patterns across this under-sampled region. Using
63 shear-wave splitting analysis of SK[K]S phase, we assess the interaction between NE-
64 oriented asthenospheric flow and the Arabian lithospheric keel, focusing specifically on the
65 Zagros foreland.

66 We consider two main geodynamic scenarios for this interaction. In the first, the thick
67 lithospheric root beneath the Zagros may force the asthenospheric flow to deeper levels,
68 allowing it to continue beneath the orogen without significant lateral deflection. In the
69 second, the lithospheric keel acts as a barrier, redirecting mantle flow laterally toward areas
70 of thinner lithosphere in adjacent regions, such as northwest Iran, eastern Anatolia, or the
71 Makran subduction zone. In addition, we evaluate the possibility of fossil anisotropy, a

72 "frozen" lithospheric fabric inherited from Mesozoic rifting events during the earlier tectonic
73 evolution of the region as part of northern Gondwana.

74 A better understanding of seismic anisotropy beneath the Zagros foreland is critical for
75 distinguishing between these scenarios and for constraining the relative contributions of
76 lithospheric and asthenospheric anisotropy. This has broader implications for understanding
77 the mechanical coupling across the Arabia–Eurasia plate boundary, the dynamics of mantle
78 flow in convergent zones, and the preservation of tectonic fabrics within stable continental
79 lithosphere. The primary objectives of this study are: (1) To determine whether seismic
80 anisotropy in the Zagros foreland originates in the lithosphere or asthenosphere; (2) To assess
81 the possible deflection or suppression of mantle flow by the lithospheric keel beneath the
82 Zagros; and (3) To investigate whether the NW–SE anisotropy observed in the
83 Mesopotamian Plain reflects fossil fabric from Mesozoic rifting.

84

85 **2. Data and method**

86 The primary dataset used in this study originates from a regional seismic network that has
87 been operational in Iraq since 2014, established through a multi-institutional collaboration
88 (Abdulnaby et al., 2020; Fig. 1). Table 1 provides the station coordinates and the time
89 intervals during which data were accessible. Most stations were repositioned over time, with
90 data collection periods ranging from five months to nine years (Table 1). To enhance lateral
91 data coverage in the Zagros foreland, we also incorporated data from a newly established
92 seismic station situated on Khark Island in the Persian Gulf. This station is operated by the
93 International Institute of Earthquake Engineering and Seismology in Iran.

94 We extracted three-component waveforms from 342 teleseismic earthquakes with magnitudes
95 ≥ 6.0 from epicentral distances between 90° and 140° . A total of 3256 seismograms met these
96 criteria. Two splitting parameters, Φ (fast-axis anisotropy orientation) and δt (splitting time
97 between fast and slow polarizations), were estimated using the rotation-correlation method of
98 Bowman and Ando (1987). Before performing the splitting analysis, we visually examined
99 the waveforms to confirm low noise levels and to ensure that the SK[K]S phases were not
100 distorted by other teleseismic phases with similar arrival times. Band-pass filtering was
101 applied using visually selected cutoff periods, with low cutoff periods ranging from 5 to 10 s
102 and high cutoff periods ranging from 20 to 30 s.

103 We manually selected the analysis window around the theoretical SK[K]S onset, calculated
104 using the IASP91 standard velocity model (Kennett and Engdahl, 1991). The window length
105 was chosen to include at least one period of the clearly observable target phases. Final
106 splitting parameters were retained in the dataset after meeting the following quality criteria:
107 (1) a signal-to-noise ratio > 2 on the radial component within the analysis window, (2) a
108 minimum correlation coefficient > 0.90 between fast and slow components, (3) elliptical
109 particle motion before correction for anisotropy and nearly linear particle motion after, and
110 (4) at least a 50% reduction in transverse energy after anisotropy correction (for non-null
111 cases). Although stricter thresholds (e.g., 70–80%) would enhance robustness, preliminary
112 tests showed they significantly reduced the number of non-null results, especially at stations
113 with lower signal quality. The 50% threshold was thus adopted as a compromise to balance
114 spatial coverage and measurement reliability.

115 Measurements with initial linear particle motion or splitting times < 0.5 s were classified as
116 null, indicating no detectable splitting. Uncertainties in fast axis orientation and splitting time
117 were estimated using the contour method, based on 95% confidence regions from the

118 normalized correlation surface. The standard deviation of splitting parameters within this
119 region was used as the uncertainty measure for each event.

120 To evaluate the robustness of our results, we reanalyzed a representative subset of events
121 using the minimum energy method. The results (Table S1, in supplementary material)
122 showed good agreement with those obtained from the rotation-correlation technique. Future
123 work incorporating full-matrix comparisons of all events using multiple methods is
124 warranted.

125 Figure 2 presents two examples of the splitting analysis, illustrating the energy on the original
126 transverse (**SH**) component and the elliptical particle motion of the horizontal components,
127 both indicative of shear wave splitting. Main criteria for reliable measurements include the
128 observation of linear particle motion and significant energy reduction on the **SH** component
129 following correction **for anisotropy** using the estimated splitting parameters. The final dataset
130 includes 155 reliable non-null measurements and 630 null measurements, as shown in
131 Figures 3 and 4.

132

133 **3. Results**

134 Figure 3 shows the rose diagrams of both null and non-null measurements for 18 new stations
135 in the Zagros foreland. **At stations AMR1, AMR2, BSR2, NSR1, NSR3, NSR4, ANB1, and**
136 **KIR1, the non-null measurements exhibit a consistent unimodal pattern (Fig. 3).** Figure 4a
137 presents the rose diagrams for non-null splitting measurements at station locations, **and**
138 **Figure 4b shows** individual measurements (represented by red bars) projected to their
139 piercing points **at a depth of 200 km**, alongside measurements from previous studies (green
140 and orange bars). **Projecting the individual measurements at depth (Fig. 4b) provides a clearer**
141 **view of the lateral distribution of anisotropy.** The figure suggests that the varying fast axis

142 orientations observed at some stations may indicate lateral variations in the anisotropic
143 structure beneath the region.

144 The fast axis orientations across the study region can be categorized into two main patterns.
145 First, in southern Iraq and the Persian Gulf (latitude $< 32^\circ\text{N}$), the orientations are
146 predominantly NW-SE, sub-parallel to the Zagros orogeny and perpendicular to the APM
147 vector within the no-net-rotation reference frame (Kreemer et al., 2014; Fig. 1). This pattern
148 is observed at stations BSR1, BSR2, NSR1, NSR2, NSR4, AMR1, AMR2, SAM2, and
149 KUT1 and extends into the Persian Gulf at station KHRK, marking the offshore continuation
150 of the Zagros foreland basin. Second, in northern Iraq (latitude $> 33^\circ\text{N}$), the fast axis
151 orientations are primarily NE-SW, perpendicular to the Zagros orogeny and sub-parallel to
152 the APM vector, as observed at stations ANB1, ANB2, KIR1, SLY1, and DHK1. Station
153 KAR2, located near the boundary between these two regions, shows almost null SK[K]S
154 splitting, with 94 null measurements and 1 non-null measurement from a west back-azimuth
155 (Fig. 3 and Table 1). This suggests the presence of two dominant anisotropic features with
156 perpendicular orientations in the northern and southern sections of the study region.

157 An important question is why a large number of null measurements (630 out of 785) are
158 observed. Figure 5 addresses this by showing polar histograms of back-azimuths for null and
159 non-null measurements across the dataset. Two dominant directions are associated with nulls:
160 east and southwest ($\approx 210^\circ$). The southwestern azimuth coincides with the fast axis orientation
161 in northern Iraq and the slow axis in southern Iraq, suggesting that SK[K]S phases from this
162 direction are polarized along the symmetry axes of anisotropy, resulting in null splitting.
163 However, the most prominent direction for nulls is from the east.

164 Station-specific back-azimuth rose diagrams (Fig. 3, right panels) show that stations AMR2,
165 BSR2, NSR1, NSR4, KUT1, KAR2, and KHRK, all located in the Mesopotamian Plain and

166 Persian Gulf, exhibit a high concentration of nulls from the east. In contrast, stations in
167 northern Iraq (e.g., ANB1, ANB2, KIR1, and SLY1) do not show a similar eastern null
168 pattern. This systematic azimuthal dependence likely results from both the complex
169 lithospheric structure east of the Mesopotamian Plain, where it interacts with the Zagros, and
170 the global distribution of teleseismic sources. A significant number of SK[K]S phases arrive
171 from the east, where active subduction zones along the western Pacific margin fall within the
172 optimal epicentral distance range for splitting analysis. Non-null measurements, by contrast,
173 predominantly arrive from other directions, especially from the west, as seen in Figure 3.

174 Figure 6 maps the lateral variation of SK[K]S splitting times across the study area and
175 surrounding region, incorporating results from this study with those from previous studies.
176 The map is generated by resampling the splitting times at regularly spaced 1° grid points and
177 averaging them over the Fresnel zone around each point. The final map is then produced by
178 linearly interpolating between the grid points. The results show that splitting times beneath
179 the Zagros foreland are generally much smaller than those reported for the surrounding
180 regions, including the Inner Arabian Platform, the eastern Anatolian Plate, and the Zagros
181 collision zone (Paul et al., 2014; Qaysi et al., 2018; Kaviani et al., 2021).

182

183 **4. Discussion**

184 The most striking feature revealed by our SK[K]S splitting observations is the relatively
185 abrupt change in anisotropy patterns across the Zagros foreland in the northeastern portion of
186 the Arabian plate. Our results reveal two distinct anisotropy regimes: a uniform NE–SW fast
187 axis orientation in the northern Iraq, aligned with the APM vector and a uniform NW–SE
188 orientation, parallel to the Zagros orogen, across the Mesopotamian Plain and Persian Gulf.
189 These coherent patterns are in sharp contrast to the complex and spatially variable anisotropy

190 within the Zagros orogen. In the following, we integrate our results with those from
191 surrounding regions to resolve anisotropic patterns on a broader scale and interpret them in
192 terms of lithosphere–asthenosphere interaction and tectonic inheritance.

193

194 **4.1 Comparison with previous studies**

195 To investigate patterns of upper mantle seismic anisotropy, we combined our dataset with all
196 available SK[K]S measurements from the Middle East. This merging allows us to assess how
197 the results of this study align with or diverge from previous observations. Figure 7 presents
198 maps comparing our measurements with those from earlier studies in neighboring regions,
199 including the Iranian Plateau and eastern Anatolian Plateau (Kaviani et al., 2021),
200 northwestern Iran (Arvin et al., 2021), the northern Zagros (Sadeghi-Bagherabadi et al.,
201 2018a, 2018b), and the Inner Arabian Platform (Qaysi et al., 2018). In the left panels of
202 Figure 7, individual SK[K]S measurements are displayed, with red bars representing the new
203 measurements and blue bars indicating those from previous studies. Each measurement is
204 projected onto its ray-piercing point at depths of 100 km, 200 km, and 300 km, shown in
205 panels a, c, and e, respectively, to account for uncertainty in the depth of anisotropy.

206 Our results show a high degree of consistency with previous measurements, particularly in
207 southern Iraq and the Persian Gulf, where NW-SE-oriented fast axes are observed. Similarly,
208 in northern Iraq, the NE-SW-oriented fast axes align well with prior measurements in
209 northern Iraq and eastern Turkey (Kaviani et al., 2021). This agreement affirms that our
210 findings extend the observation of upper mantle anisotropy across the Zagros collision zone
211 and enhance understanding of mantle flow and deformation beneath this tectonically active
212 region.

213 To further visualize the azimuthal anisotropy patterns, we calculated vector averages of the
214 individual splitting parameters projected at respective depths and within the Fresnel zone of
215 SK[K]S waves, utilizing sensitivity kernels as calculated by Monteiller and Chevrot (2011).
216 The interpolated anisotropy fields, shown in the right panels of Figure 7, demonstrate that the
217 anisotropic patterns remain largely consistent across different depth levels. **The observed**
218 **consistency in fast-axis orientations across depth projections suggests a dominantly single-**
219 **layer anisotropic structure.**

220

221 **4.2 Uniform asthenospheric flow around the Arabian–Eurasian collision zone**

222 **In the northern Arabian Plate and much of the Eurasian Plate, the fast axes of SK[K]S**
223 **splitting are consistently aligned with the APM direction of the Arabian Plate (Figs. 4 and 7).**
224 **These regions also exhibit relatively large splitting delay times (Fig. 6), suggesting a strong**
225 **and coherent anisotropic signal.** The uniform pattern of fast axes over such a broad region
226 suggests a large-scale, viscous asthenosphere flow as the dominant mechanism beneath the
227 northern Middle East (Sandvol et al., 2003; Paul et al., 2014). **This flow is aligned with the**
228 **APM direction and appears to be only weakly influenced by lithospheric heterogeneities.**

229 **This interpretation is supported by previous studies, which report similar trends in anisotropy**
230 **fast axis orientation and large splitting delay times across central Anatolia, eastern Turkey,**
231 **and beneath northwestern and northeastern Iran (Sandvol et al., 2003; Paul et al., 2014;**
232 **Kaviani et al., 2021; Arvin et al., 2021).** In some locations, splitting observations vary with
233 back-azimuth, indicating contributions from multiple layers of anisotropy at different depths.
234 **This vertical complexity suggests that distinct layers within the lithosphere–asthenosphere**
235 **system contribute different anisotropic signatures.**

236 The asthenospheric origin of the observed SK[K]S anisotropy is further supported by
237 lithospheric thickness estimates from surface wave tomography (Priestley et al., 2012) and S
238 receiver function studies (Gök et al., 2007; Taghizadeh-Farahmand et al., 2010 and 2013;
239 Kind et al., 2015). These studies reveal a thin lithosphere beneath regions where the fast axis
240 orientations are coherently aligned with the APM. The lithospheric thickness ranges from
241 ~80 to 100 km beneath eastern Anatolia and the Bitlis suture zone (e.g., Kind et al., 2015),
242 northwestern Iran (e.g., Taghizadeh-Farahmand et al., 2010), and northeastern Iran (e.g.,
243 Taghizadeh-Farahmand et al., 2013). In some parts of the Anatolian Plate, the lithospheric
244 mantle is reportedly entirely absent (e.g., Gök et al., 2007).

245 It is noteworthy that the tectonics of northern Iraq and eastern Turkey are dominated by the
246 active convergence between the Arabian and Eurasian plates, accommodated by the westward
247 escape of Anatolia (Dewey et al., 1986; McClusky et al., 2000). Despite the complex and
248 ongoing deformation at this junction, the anisotropy patterns remain remarkably consistent
249 and unperturbed. This may confirm that the overlying lithosphere is not sufficiently thick to
250 significantly influence the underlying mantle flow. Alternatively, any lithospheric fabrics that
251 may be present could be aligned with the underlying mantle flow, resulting in a vertically
252 coherent anisotropic signal that is indistinguishable from asthenospheric anisotropy in
253 SK[K]S splitting data. The alignment between surface tectonic motions and the orientation of
254 asthenospheric flow further supports a strong coupling between the thin lithosphere and
255 underlying mantle, reinforcing the interpretation that asthenospheric flow is the dominant
256 driver of plate tectonics in this region.

257

258 **4.3 Lithospheric control and fossil anisotropy in the Zagros foreland**

259 In contrast to the uniform patterns observed farther north, the SKS splitting beneath the
260 Zagros collision zone and the Mesopotamian foreland displays a more complex and spatially
261 variable character. The fast axis orientations in this region are deflected around the Zagros
262 lithospheric keel and the Mesopotamian foreland, while the splitting delay times are smaller
263 than those in the surrounding areas. These patterns have been interpreted as resulting from
264 mantle flow deflection around the thick Zagros lithospheric root (e.g., Kaviani et al., 2021).

265 We interpret these patterns in the context of lithosphere-asthenosphere interaction and
266 propose that the cold, thick Arabian lithosphere beneath the Zagros foreland and Zagros
267 orogeny both disrupts mantle flow and inhibits the development of coherent anisotropic
268 fabrics within itself and in the underlying asthenosphere. This interpretation is supported by
269 the correlation between anisotropy orientations and lithospheric thickness contours (Fig. 8d),
270 and by thermal models indicating sub-Moho temperatures below 900°C (Priestley et al.,
271 2012), which limit olivine mobility and the formation of vertically coherent lattice-preferred
272 orientation in the lithosphere due to pure-shear deformation during the collision (Nicolas and
273 Christensen, 1987).

274 The relatively small splitting times beneath the Mesopotamian Plain support the idea that
275 anisotropy in this region is either weak or confined to a shallow layer. We suggest that the
276 source of anisotropy resides in the upper lithospheric mantle and reflects a fossil fabric as a
277 remnant of early Mesozoic rifting that affected the northeastern Arabian platform. This
278 interpretation is supported by two main lines of evidence: (1) A strong correlation between
279 the SK[K]S fast axis orientation and the Pn fast axis anisotropy orientation (Fig. 8c), which
280 represent subcrustal anisotropy, suggesting a shallow origin; (2) Small-scale lateral variations
281 in anisotropy directions beneath the Mesopotamian Plain, in contrast to the more uniform
282 patterns beneath the Inner Arabian platform and eastern Anatolia (see interpolated anisotropy
283 fields in Fig. 7).

284 Our findings suggest that the NW–SE fast-axis anisotropy within the lithosphere of the
285 Mesopotamian Plain likely originates from successive Mesozoic rifting events affecting the
286 northeastern Arabian platform. Evidence for diffuse rifting in the region comes from previous
287 geological and seismological studies (Mohammed, 2006; Numan, 1997, 2000; Jassim and
288 Göff, 2006; Abdalnaby et al., 2020). P receiver function analysis (Abdalnaby et al., 2020)
289 revealed a crustal root beneath the southeastern Mesopotamian Plain comparable in thickness
290 to that of the Zagros collision zone. Abdalnaby et al. (2020) attributed the mismatch between
291 large crustal thickness and low topography to successive rifting events, which promoted
292 vertical loading from up to 14 km of sediment accumulation in fault-bounded depocenters.
293 The Abu Jir-Euphrates fault, clearly imaged as a basement step in seismic lines (Mohammed,
294 2006), defines the southwest margin of the rift system (e.g., Fadhel and Al-Rahim, 2019).
295 Inherited from Triassic passive-margin extension, this fault system was reactivated during
296 Middle–Late Jurassic rifting, forming graben–horst structures (Numan, 1997, 2000).
297 Continuous subsidence since the Late Jurassic enabled the deposition of thick sedimentary
298 sequences within the Mesopotamian Plain (Jassim and Göff, 2006).

299 The lithosphere beneath the Mesopotamian Plain appears to have remained largely intact
300 despite the subsequent continental collision and deformation associated with the advancing
301 Zagros deformation front. The southwestward migration of the Zagros deformation front
302 (ZFF) overprinted the eastern boundary of the Mesopotamian graben through thrust faulting
303 and folding, producing opposing dips in the sedimentary cover. Abdalnaby et al. (2016a,
304 2016b) and Darweesh et al. (2017) proposed a southwestward dip of approximately 60° for
305 the eastern margin of the basin beneath the ZFF. Collectively, these findings support the
306 interpretation that the Mesopotamian Plain has been largely unaffected by deformation
307 associated with the Zagros orogeny. As a result, older tectonic processes, most notably

308 Mesozoic rifting, are the most plausible source of the preserved lithospheric mantle
309 anisotropy.

310 While this interpretation is supported by multiple lines of evidence, forward modeling of
311 shear-wave propagation through synthetic anisotropic structures will be critical to constrain
312 the symmetry and depth extent of the anisotropy in the Mesopotamian lithosphere. The high
313 occurrence of null measurements from the east may indicate a complex interaction between
314 the lithosphere and asthenosphere at the boundary between Mesopotamia and the Zagros. A
315 plausible explanation for these nulls is a two-layer anisotropic structure with orthogonal fast
316 orientations, where the opposing effects of each layer interfere destructively. Such a
317 configuration could result in the observed nulls for eastward-arriving waves across the
318 Mesopotamian plain.

319

320 **5. Conclusions**

321 This study provides new SK[K]S splitting measurements from 18 seismic stations in the
322 foreland of the Zagros collision zone, helping to fill a major gap in anisotropy coverage
323 across the Middle East. The dataset reveals two distinct anisotropy domains: a NE–SW fast-
324 axis orientation in northern Iraq, and a NW–SE orientation beneath the Mesopotamian Plain
325 and Persian Gulf. The NE–SW orientation aligns with the direction of absolute plate motion,
326 suggesting that large-scale asthenospheric flow, coupled with the overlying lithosphere,
327 governs anisotropy in northern Iraq and the broader northern Middle East. In contrast, the
328 NW–SE fast axis orientations and smaller splitting times beneath the Mesopotamian Plain
329 and Persian Gulf indicate a shallow lithospheric source, likely reflecting a fossil fabric from
330 Mesozoic rifting. The cold, thick Arabian lithosphere beneath the Zagros foreland further
331 disrupts mantle flow and suppresses the formation of coherent anisotropic fabrics, both

332 within itself and in the underlying asthenosphere. These findings highlight the joint control of
333 lithospheric structure and mantle dynamics on seismic anisotropy in a continental collision
334 zone. They emphasize the importance of inherited lithospheric fabrics, thermal structure, and
335 lithosphere–asthenosphere coupling in shaping observed anisotropic patterns.

336

337 **Acknowledgements**

338 We are grateful to the Lawrence Livermore National Laboratory (LLNL) for supporting the
339 installation of broadband seismic stations in Iraq. We also like to thank the University of
340 Arkansas, Little Rock, for partially supporting this research.

341 **Data availability**

342 Continuous data from 17 Iraqi stations used in this study are available through the
343 Incorporated Research Institutions for Seismology (IRIS).

344 **Author contribution**

345 KM analyzed the data, prepared figures, interpreted the results, and wrote the initial draft of
346 the manuscript. AK developed the code, supervised the data analysis, prepared figures, and
347 revised the manuscript. WA conducted the field survey, collected raw data, provided the data,
348 and revised the manuscript. HM secured funding for data collection in Iraq and revised the
349 manuscript. HA secured funding for data collection in Iraq and revised the manuscript.

350 **Competing interests**

351 None of the authors has any competing interests.

352

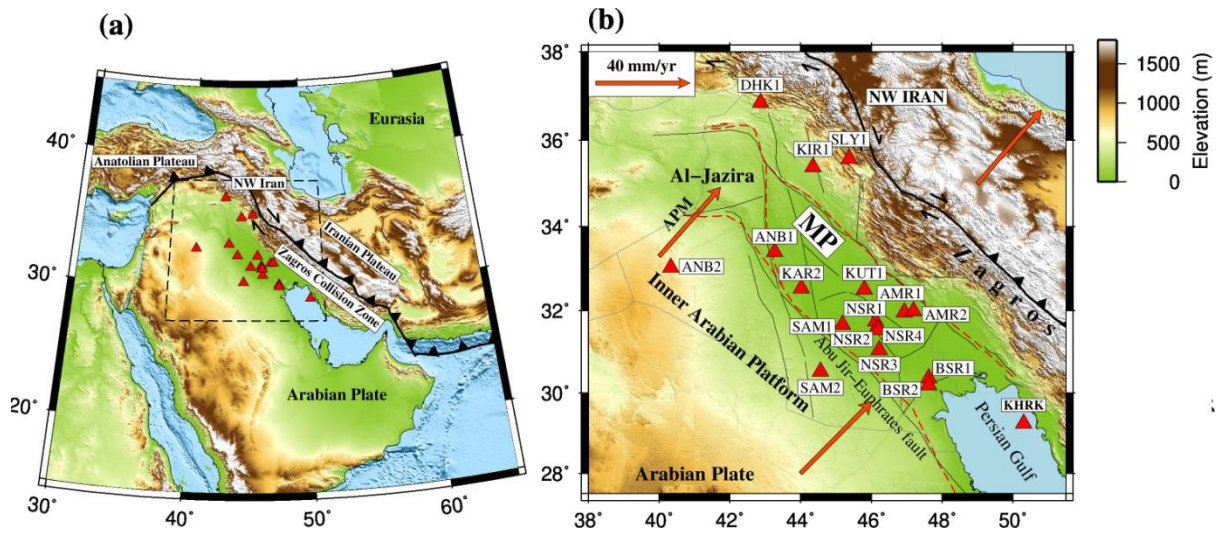
353 **References**

- 354 Abdalnaby, W., Al-Mohmed, R., & Mahdi, M. (2016a). Seismicity and recent stress regime
355 of Diyala City, Iraq–Iran border. *Modeling Earth Systems and Environment*, 2, 1-8.
- 356 Abdalnaby, W., Mahdi, M., Al-Mohmed, R., & Mahdi, H. H. (2016b). Seismotectonic of
357 Badra-Amarah Fault, Iraq-Iran border. *IOSR Journal of Applied Geology and*
358 *Geophysics (IOSR-JAGG)*, 4(3), 27-33.
- 359 Abdalnaby, W., Motaghi, K., Shabanian, E., Mahdi, H., Al-Shukri, H., & Gök, R. (2020).
360 Crustal structure of the Mesopotamian Plain, east of Iraq. *Tectonics*, 39(11),
361 e2020TC006225.
- 362 Arvin, S., Sobouti, F., Priestley, K., Ghods, A., Motaghi, K., Tilmann, F., & Eken, T. (2021).
363 Seismic anisotropy and mantle deformation in NW Iran inferred from splitting
364 measurements of SK (K) S and direct S phases. *Geophysical Journal International*,
365 226(2), 1417-1431.
- 366 Bowman, J. R., & Ando, M. (1987). Shear-wave splitting in the upper-mantle wedge above
367 the Tonga subduction zone. *Geophysical Journal International*, 88(1), 25-41.
- 368 Celli, N. L., Lebedev, S., Schaeffer, A. J., & Gaina, C. (2020). African cratonic lithosphere
369 carved by mantle plumes. *Nature communications*, 11(1), 92.
- 370 Darweesh, H. A., Obed, A. Z. M., & Albadran, B. N. (2017). Structural study of basins
371 configuration in Mesopotamian area. *International journal of engineering and applied*
372 *sciences*, 4(9), 54-58.
- 373 Dewey, J. F., Hempton, M. R., Kidd, W. S. F., Saroglu, F. A. M. C., & Şengör, A. M. C.
374 (1986). Shortening of continental lithosphere: the neotectonics of Eastern Anatolia—a
375 young collision zone. *Geological Society, London, Special Publications*, 19(1), 1-36.
- 376 Fadhel, M. S., & Al-Rahim, A. M. (2019). A new tectono sedimentary framework of the
377 Jurassic succession in the Merjan oil field, Central Iraq. *Journal of Petroleum*
378 *Exploration and Production Technology*, 9(4), 2591-2603.
- 379 Fouad, S. F. (2010a). Tectonic evolution of the Mesopotamia Foredeep in Iraq. *Iraqi Bulletin*
380 *of Geology and Mining*, 6(2), 41–53.
- 381 Fouad, S. F. (2010b). Tectonic map of Iraq, Scale 1: 1000 000 (3rd ed.). Baghdad, Iraq:
382 Geological Survey and Mineral Investigation (GEOSURV).
- 383 Gök, R., Pasyanos, M. E., & Zor, E. (2007). Lithospheric structure of the continent—
384 continent collision zone: eastern Turkey. *Geophysical Journal International*, 169(3),
385 1079-1088.
- 386 Jassim, S. Z., & Göff, J. C. (2006). *Geology of Iraq*. Dolin, Prague and Moravian Museum,
387 Brno, Czech Republic, p. 341.
- 388 Kaviani, A., Mahmoodabadi, M., Rumpker, G., Pilia, S., Tatar, M., Nilfouroushan, F., ... &
389 Ali, M. Y. (2021). Mantle-flow diversion beneath the Iranian plateau induced by Zagros’
390 lithospheric keel. *Scientific reports*, 11(1), 2848.

- 391 Kennett, B. L. N., & Engdahl, E. R. (1991). Traveltimes for global earthquake location and
392 phase identification. *Geophysical Journal International*, 105(2), 429-465.
- 393 Kind, R., Eken, T., Tilmann, F., Sodoudi, F., Taymaz, T., Bulut, F., ... & Schneider, F.
394 (2015). Thickness of the lithosphere beneath Turkey and surroundings from S-receiver
395 functions. *Solid Earth*, 6(3), 971-984.
- 396 Kreemer, C., Blewitt, G. & Klein, E.C., (2014). A geodetic plate motion and Global Strain
397 Rate Model, *Geochem., Geophys., Geosyst.*, 15(10), 3849–3889.
- 398 Long, M. D., & Becker, T. W. (2010). Mantle dynamics and seismic anisotropy. *Earth and
399 Planetary Science Letters*, 297(3-4), 341-354.
- 400 Lü, Y., Ni, S., Chen, L., & Chen, Q. F. (2017). Pn tomography with Moho depth correction
401 from eastern Europe to western China. *Journal of Geophysical Research: Solid Earth*,
402 122(2), 1284-1301.
- 403 McClusky, S., Balassanian, S., Barka, A., Demir, C., Ergintav, S., Georgiev, I., ... & Veis, G.
404 (2000). Global Positioning System constraints on plate kinematics and dynamics in the
405 eastern Mediterranean and Caucasus. *Journal of Geophysical Research: Solid Earth*,
406 105(B3), 5695-5719.
- 407 Mohammed, S. A. (2006). Megaseismic section across the northeastern slope of the Arabian
408 Plate, Iraq. *GeoArabia*, 11(4), 77-90.
- 409 Monteiller, V., and S. Chevrot, 2011. High-resolution imaging of the deep anisotropic
410 structure of the San Andreas Fault system beneath southern California, *Geophys. J. Int.*,
411 186, 418-446
- 412 Nicolas, A., & Christensen, N. I. (1987). Formation of anisotropy in upper mantle peridotites-
413 A review. Composition, structure and dynamics of the lithosphere-asthenosphere system,
414 16, 111-123.
- 415 NOAA National Centers for Environmental Information, (2022). ETOPO 2022 15 Arc-
416 Second Global Relief Model. NOAA National Centers for Environmental Information.
- 417 Numan, N. M. S. (1997). A plate tectonic scenario for the phanerozoic succession in Iraq.
418 *Journal of the Geological Society of Iraq*, 30(2), 85–110.
- 419 Numan, N. M. S. (2000). Major cretaceous tectonic events in Iraq. *Rafidain Journal of
420 Science*, 11(3), 32–52.
- 421 Park, J., & Levin, V. (2002). Seismic anisotropy: tracing plate dynamics in the mantle.
422 *Science*, 296(5567), 485-489.
- 423 Paul, A., Karabulut, H., Mutlu, A. K., & Salaün, G. (2014). A comprehensive and densely
424 sampled map of shear-wave azimuthal anisotropy in the Aegean–Anatolia region. *Earth
425 and Planetary Science Letters*, 389, 14-22.
- 426 Priestley, K., McKenzie, D., Barron, J., Tatar, M., & Debayle, E. (2012). The Zagros core:
427 Deformation of the continental lithospheric mantle. *Geochemistry, Geophysics,
428 Geosystems*, 13(11).

- 429 Priestley, K., & McKenzie, D. (2013). The relationship between shear wave velocity,
430 temperature, attenuation and viscosity in the shallow part of the mantle. *Earth and*
431 *Planetary Science Letters*, 381, 78-91.
- 432 Qaysi, S., Liu, K. H., & Gao, S. S. (2018). A database of shear-wave splitting measurements
433 for the Arabian Plate. *Seismological Research Letters*, 89(6), 2294-2298.
- 434 Sadeghi-Bagherabadi, A., Sobouti, F., Ghods, A., Motaghi, K., Talebian, M., Chen, L., ... &
435 He, Y. (2018a). Upper mantle anisotropy and deformation beneath the major thrust-and-
436 fold belts of Zagros and Alborz and the Iranian Plateau. *Geophysical Journal*
437 *International*, 214(3), 1913-1918.
- 438 Sadeghi-Bagherabadi, A., Margheriti, L., Aoudia, A., & Sobouti, F. (2018b). Seismic
439 anisotropy and its geodynamic implications in Iran, the easternmost part of the Tethyan
440 Belt. *Tectonics*, 37(12), 4377-4395.
- 441 Sandvol, E., Turkelli, N., Zor, E., Gök, R., Bekler, T., Gurbuz, C., ... & Barazangi, M. (2003).
442 Shear wave splitting in a young continent-continent collision: An example from eastern
443 Turkey. *Geophysical Research Letters*, 30(24).
- 444 Silver, P. G., & Chan, W. W. (1991). Shear wave splitting and subcontinental mantle
445 deformation. *Journal of Geophysical Research: Solid Earth*, 96(B10), 16429-16454.
- 446 Silver, P. G., & Holt, W. E. (2002). The mantle flow field beneath western North America.
447 *Science*, 295(5557), 1054-1057.
- 448 Sissakian, V., Shihab, A. T., Al-Ansari, N., & Knutsson, S. (2017). New tectonic finding and
449 its implications on locating Oilfields in parts of the Gulf region. *Journal of Earth*
450 *Sciences and Geotechnical Engineering*, 7(3), 51-75.
- 451 Taghizadeh-Farahmand, F., Sodoudi, F., Afsari, N., & Ghassemi, M. R. (2010). Lithospheric
452 structure of NW Iran from P and S receiver functions. *Journal of seismology*, 14, 823-
453 836.
- 454 Taghizadeh-Farahmand, F., Sodoudi, F., Afsari, N., & Mohammadi, N. (2013). A detailed
455 receiver function image of the lithosphere beneath the Kopeh-Dagh (Northeast Iran).
456 *Journal of seismology*, 17, 1207-1221.
- 457
- 458

459 **Figure 1**



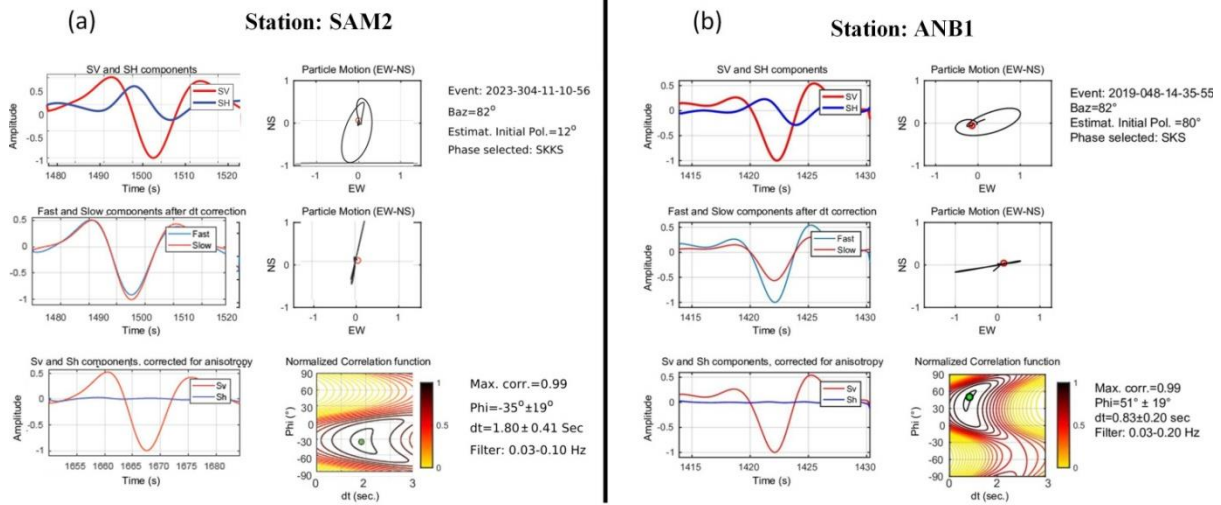
460

461

462 **Figure 1:** (a) Topographic Map of the Middle East. The triangles indicate the locations of 18
463 seismic stations within the study area. The solid line marks the Bitlis-Zagros suture boundary.
464 The dashed-line rectangle outlines the boundaries of the map displayed in panel (b). (b)
465 Topographic Map of Mesopotamian Foredeep, situated in the foreland of the Zagros collision
466 zone. The red dashed line indicates the tectonic division of Iraq as proposed by Fouad
467 (2010a, 2010b) and Sissakian et al. (2017), separating the Inner Arabian Platform from the
468 Outer Arabian Platform, which includes the Mesopotamian Foredeep, Al-Jazira, and Zagros
469 collision zone. Arrows represent the absolute plate motion (APM) vectors from Kremer et
470 al. (2014). Thin black lines mark the location of basement faults within the Zagros Foreland
471 Basin. Topographic and bathymetric data were obtained from the ETOPO1 global relief
472 model (NOAA NCEI, 2022).

473

474 **Figure 2**



475

476 **Figure 2:** Examples of shear-wave splitting measurements using the rotation-correlation

477 method. The locations of the two stations can be inferred from Figure 1b. (a) Single-event

478 measurement at station SAM2. Data have been filtered to retain periods between 10 and 30 s.

479 Information about the event is provided in the top right corner. The left panels, from top to

480 bottom, display the original radial (red) and transverse (blue) seismograms, corrected fast

481 (blue) and slow (red) components, and corrected radial (red) and transverse (blue)

482 components, respectively. The right panels, from top to bottom, show the initial particle

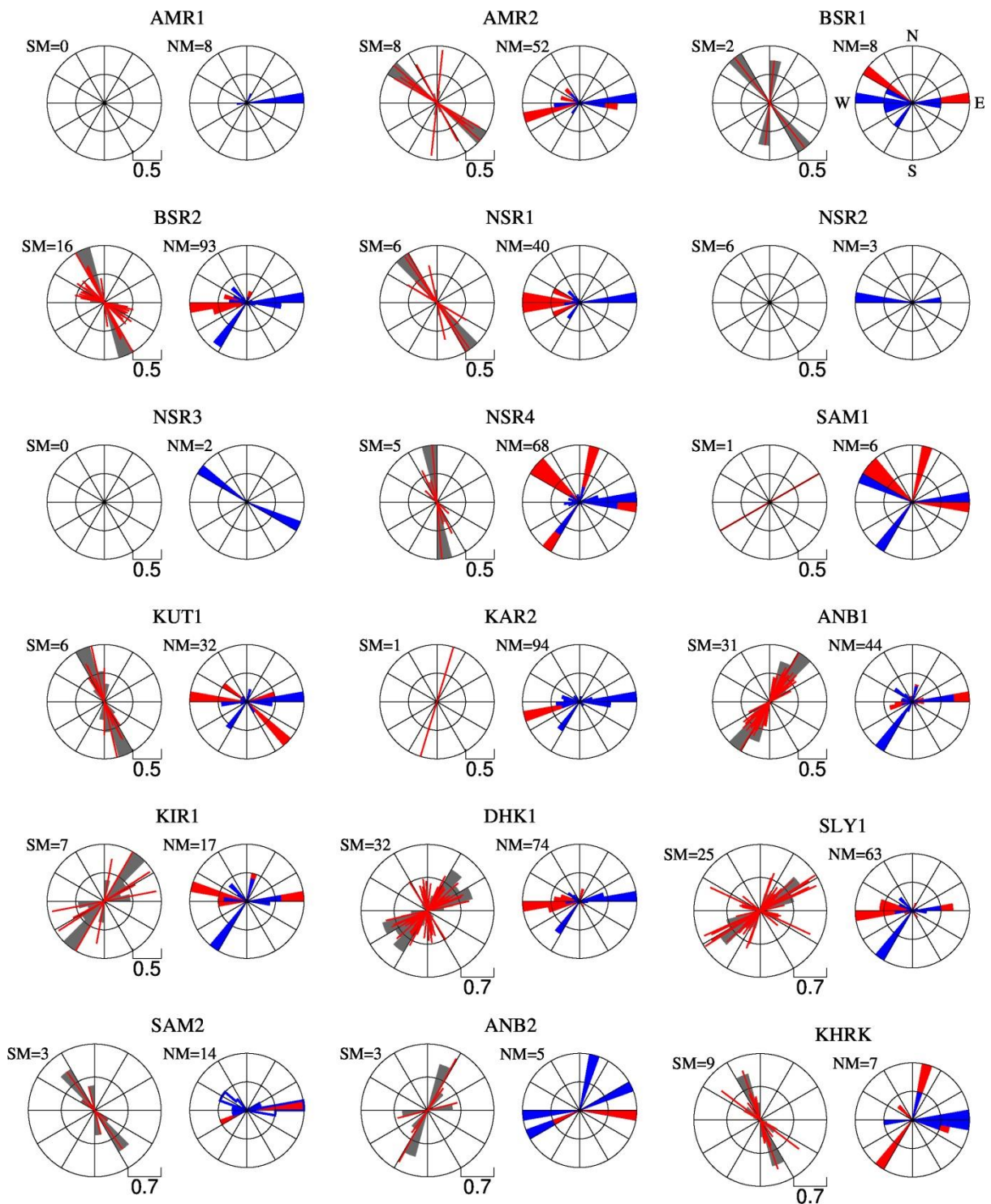
483 motion, the corrected particle motion, and the contour plot of the normalized correlation

484 function with the optimal splitting parameter indicated by a green circle. The obtained

485 splitting parameters are written in the bottom right corner. (b) Similar to (a) but for station

486 ANB1.

487

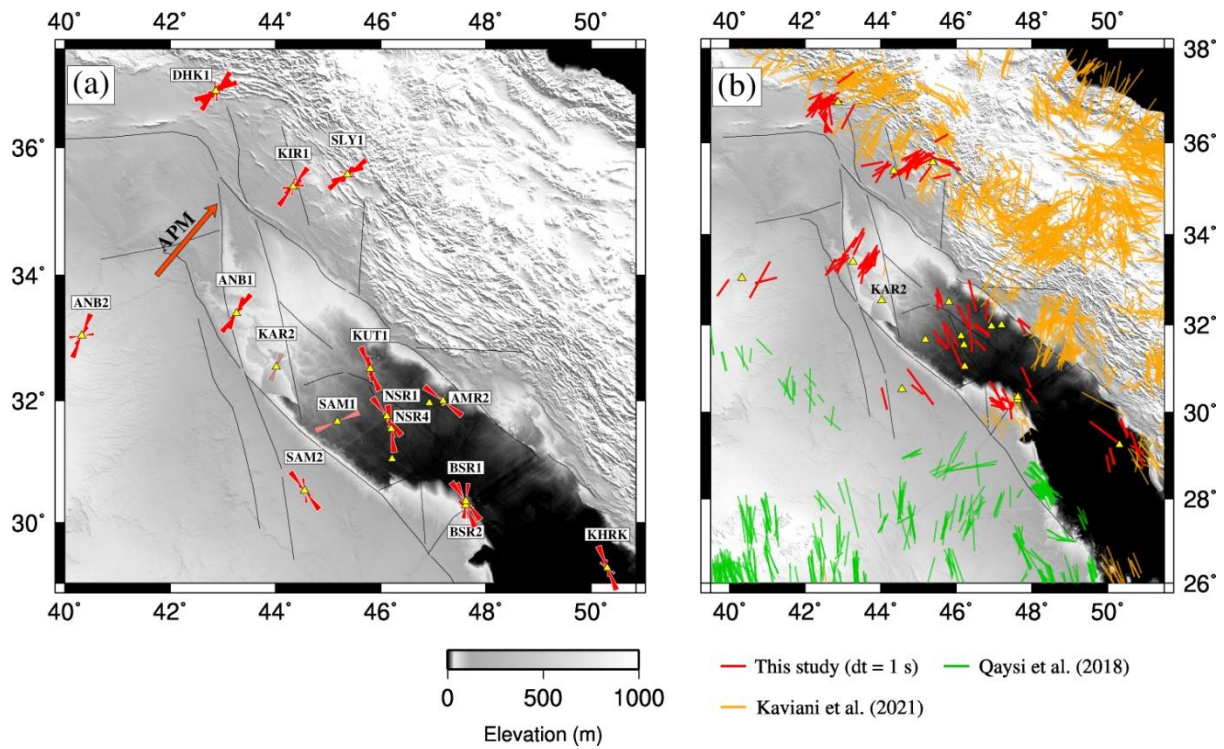


489 **Figure 3:** Rose plots of splitting measurements for stations used in this study. For each sta-
 490 tion, non-null measurements are shown on the left-hand side plot as red bars oriented in the
 491 fast direction with length proportional to the lag time. **Gray wedges represent histograms of**
 492 **individual measurements, binned in 15° sectors. Rose diagram of the initial polarization di-**
 493

494 rections of null and non-null measurements are respectively shown as blue and red wedges on
495 the right-hand side plots. Station locations are shown in Figure 1. NM: number of null meas-
496 urements; SM: number of splitting measurements.

497

498 **Figure 4**



499

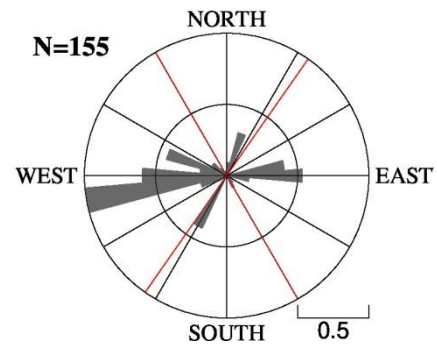
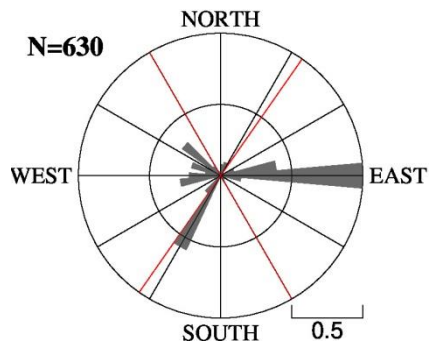
500 **Figure 4:** (a) Rose plot for non-null splitting measurements at seismic station locations
501 (triangles). Measurements for stations SAM2 and KAR2 are shown in pink, as each has only
502 one non-null observation. Arrow represent absolute plate motion (APM) vector from
503 Kreemer et al. (2014). (b) Individual fast-axis orientations from this study (red bars) and
504 previous studies by Qaysi et al. (2018) and Kaviani et al. (2021), projected onto the ray-
505 piercing points at a depth of 200 km. Topographic and bathymetric data were obtained from
506 the ETOPO1 global relief model (NOAA NCEI, 2022).

507

508 **Figure 5**

(a) Null Measurements

(b) Non-null Measurements



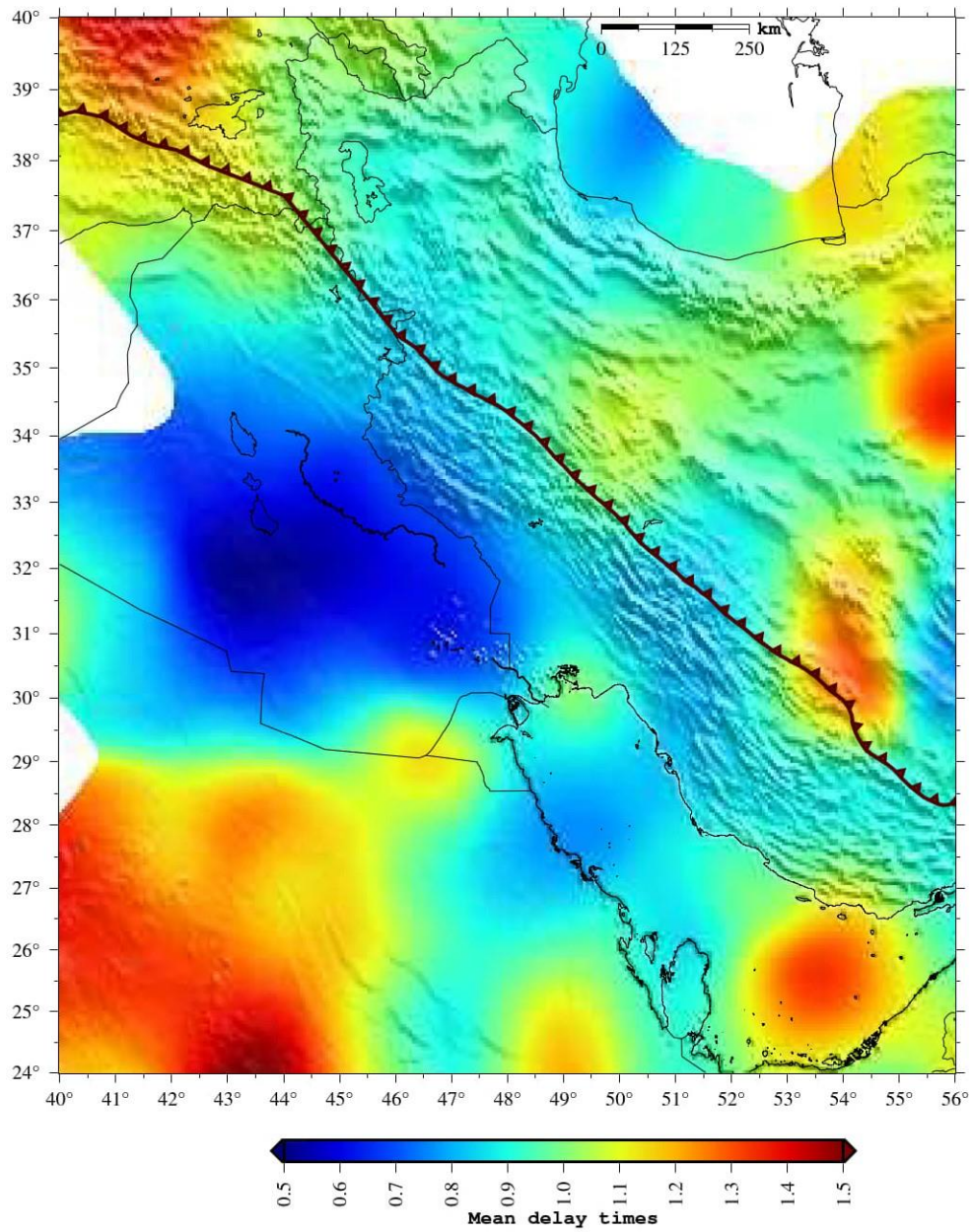
509

510 **Figure 5:** Rose plots of back-azimuths for (a) null and (b) non-null measurements, binned in
511 10° sectors. Red lines indicate the fast axis orientations of anisotropy in northern and south-
512 ern Iraq. N denotes the number of measurements used to plot the rose diagrams.

513

514

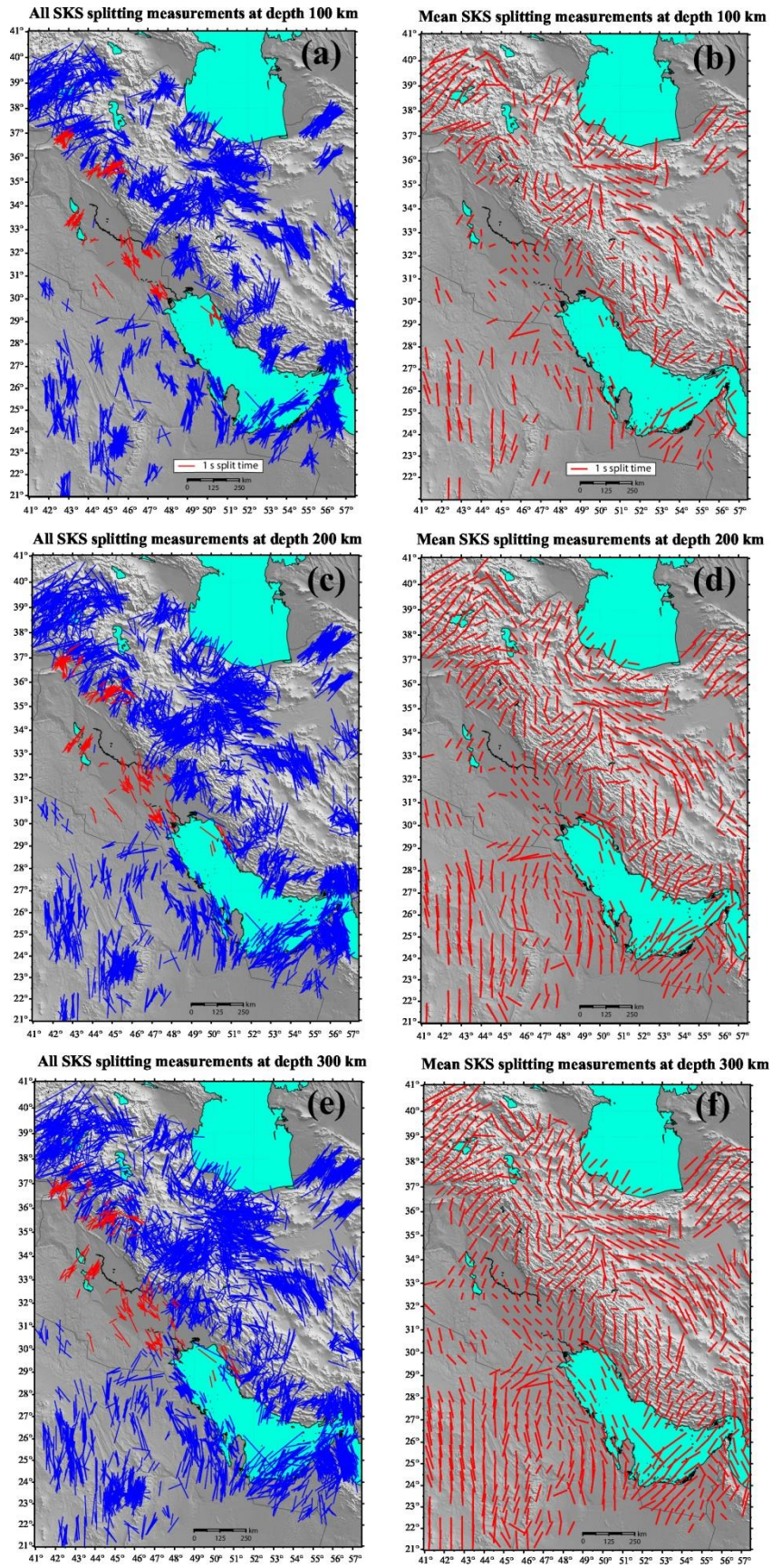
515 **Figure 6**



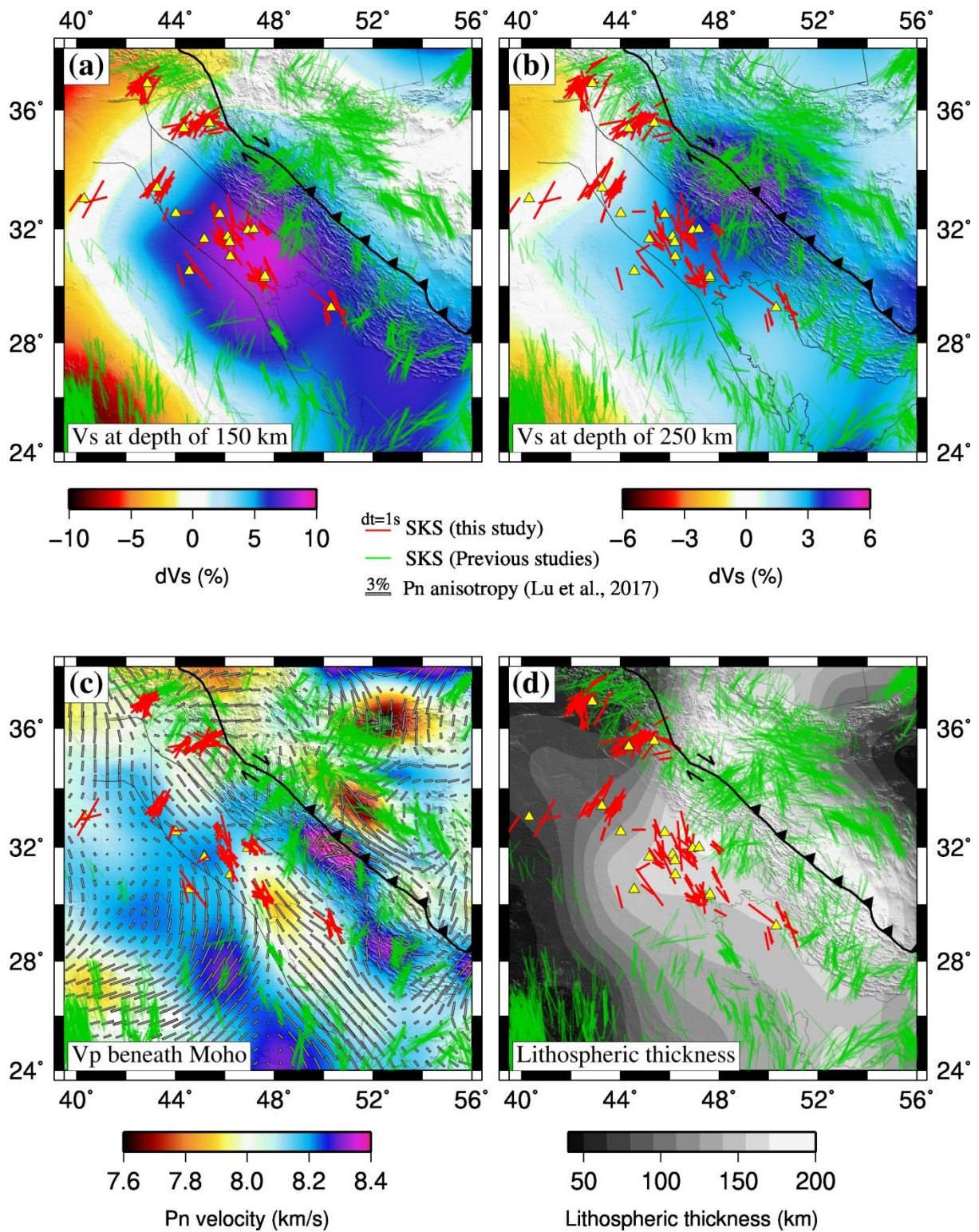
516

517 **Figure 6:** Spatial distribution of SKS splitting times across the Zagros foredeep and
518 surrounding regions, based on data from this study and previous works. The map is generated
519 by resampling the splitting times at regularly spaced 1° grid points, averaging over the
520 Fresnel zone around each point, and linearly interpolating between the grid points.

521



525 **Figure 7:** Anisotropic fast axis orientations from the current study (depicted by red bars in
526 the left panels) combined with prior measurements (represented by blue bars) from Kaviani et
527 al. (2021), Arvin et al. (2021), Sadeghi-Bagherabadi et al. (2018a and 2018b), and Qaysi et
528 al. (2018). The left panels illustrate the fast axis orientations projected onto the ray-piercing
529 point at depths of (a) 100 km, (c) 200 km, and (e) 300 km. The right panels display
530 interpolated anisotropy fields at depths of (b) 100 km, (d) 200 km, and (f) 300 km. Elevation
531 data were derived from ETOPO1 (NOAA NCEI, 2022).



533

534 **Figure 8:** (a) Shear-wave velocity (V_s) map at a depth of 150 km from regional full-
 535 waveform tomography by Celli et al. (2020). Colored bars represent individual fast-axis
 536 orientations from this study and previous studies, projected onto ray-piercing points at a

537 depth of 150 km. Thin black lines mark the borders of Mesopotamian Foredeep and Al-Jazira
538 (Sissakian et al., 2017). (b) Same as (a), but at a depth of 250 km. (c) Pn velocity map with
539 fast-axis anisotropy orientations (gray bars) from Lü et al. (2017), overlaid with individual
540 fast-axis orientation measurements projected to a depth of 75 km. (d) Lithospheric thickness
541 map from Priestley and McKenzie (2013), with colored bars representing the individual fast-
542 axis orientations projected onto ray-piercing points at a depth of 250 km. Elevation data were
543 derived from ETOPO1 (NOAA NCEI, 2022).

544

545

546 **Table 1.** Summary of the used stations in this study and their splitting parameters. The table
547 shows the station location, the circular mean of the fast axis orientation ($\bar{\varphi}$), the mean
548 splitting time ($\bar{\delta t}$), the number of splitting measurements (SM), and the number of null
549 measurements (NM). Stations with bimodal fast axis orientations are marked with an asterisk
550 (*).

Station	Latitude	Longitude	Begin date (YYYY/MM)	End date (YYYY/MM)	$\bar{\varphi}$ (o)	$\bar{\delta t}$ (s)	SM	NM
AMR1	31.9590	46.9286	2015/03	2015/10	-	-	0	8
AMR2	31.9899	47.1902	2015/11	2022/08	$-42^\circ \pm 21^\circ$	0.65 ± 0.12	8	52
ANB1	33.401	43.2576	2018/10	present	$32^\circ \pm 10^\circ$	0.76 ± 0.19	31	44
ANB2	33.0375	40.320	2023/06	present	$42^\circ \pm 20^\circ$	1.15 ± 0.51	3	5
BSR1*	30.3581	47.6153	2014/08	2015/08	$-19^\circ \pm 22^\circ$	0.61 ± 0.13	2	8
BSR2	30.2927	47.6191	2015/09	present	$-43^\circ \pm 20^\circ$	0.70 ± 0.21	16	93
DHK1*	36.8606	42.8665	2014/01	present	$38^\circ \pm 30^\circ$	0.81 ± 0.20	32	74
KAR2	32.5398	44.0224	2017/01	2023/02	$17^\circ \pm 28^\circ$	0.52 ± 0.62	1	94
KIR1	35.388	44.3419	2018/09	2021/08	$44^\circ \pm 23^\circ$	0.74 ± 0.20	7	17
KHRK	29.2543	50.3133	2021/04	present	$-29^\circ \pm 16^\circ$	0.86 ± 0.36	9	7
KUT1	32.509	45.797	2021/11	2023/02	$-19^\circ \pm 10^\circ$	0.87 ± 0.26	6	32
NSR1	31.7416	46.1151	2014/08	2017/09	$-35^\circ \pm 13^\circ$	0.69 ± 0.21	6	40
NSR2	31.5550	46.1374	2014/07	2014/09	-	-	0	3
NSR3	31.0514	46.2199	2014/07	2014/11	-	-	0	2
NSR4	31.540	46.202	2017/10	present	$-16^\circ \pm 13^\circ$	1.02 ± 0.61	5	68
SAM1	31.661	45.183	2020/12	2021/11	$60^\circ \pm 37^\circ$	0.51 ± 0.77	1	6
SAM2	30.5295	44.5587	2023/03	present	$-33^\circ \pm 13^\circ$	1.12 ± 0.62	3	14
SLY1	35.5784	45.3667	2015/09	present	$38^\circ \pm 47^\circ$	0.98 ± 0.44	25	63

551